Catalysis Science & Technology

ROYAL SOCIETY OF CHEMISTRY

PAPER

View Article Online
View Journal | View Issue

Cite this: *Catal. Sci. Technol.*, 2022, 12, 2462

Effects of high-temperature CeO_2 calcination on the activity of Pt/CeO_2 catalysts for oxidation of unburned hydrocarbon fuels

Fan Lin,[a] Kenneth Rappé,[a] Libor Kovarik,[a] Miao Song,[a] Xiaohong Shari Li,[a] Mark Engelhard[a] and Yong Wang *[ab]

Received 7th January 2022,
Accepted 6th February 2022

DOI: 10.1039/d2cy00030j

rsc.li/catalysis

A CeO_2-supported Pt catalyst (denoted $Pt/CeO_2(800)$) was prepared by pre-calcining a commercial CeO_2 support at high temperature (800 °C) before loading Pt *via* the incipient wetness impregnation method. $Pt/CeO_2(800)$ exhibits enhanced redox and hydrocarbon (HC) oxidation activity, in comparison to a catalyst with untreated CeO_2 support (denoted $Pt/CeO_2(UT)$). A combination of multiple characterization techniques, including X-ray diffraction (XRD), transmission electron microscopy (TEM), CO temperature-programed reduction (CO-TPR), and diffuse reflectance infrared Fourier transform spectroscopy (DRIFTS), shows that the promoted redox activity of $Pt/CeO_2(800)$ is independent of the morphology of Pt clusters. Instead, it is associated with the enhanced mobility of surface lattice oxygen on the high temperature pretreated CeO_2 support. The catalysts were evaluated for the catalytic oxidation of various HC fuel blendstocks with different functionalities (C=C, C–O, and C=O bonds) under different simplified and simulated exhaust conditions (with 0.74% and 10% O_2). Under simulated exhaust conditions, fuel molecules, regardless of functionalities, are always more active under lean (high O_2) conditions than under rich (low O_2) conditions although their oxidation reactivity is suppressed by the competitive adsorption of NO and CO. The high redox activity of $Pt/CeO_2(800)$ facilitates the HC oxidation by accelerating the rate-limiting O_2 activation step and broadening the operation window for an oxygen-dominant Pt surface.

Introduction

The Co-optimization of Fuels and Engines (Co-Optima) initiative by the U.S. Department of Energy aims to simultaneously develop highly efficient advanced engines along with high-performance fuels to reduce petroleum consumption. Emerging multimode engine technologies offer higher efficiency by combining spark ignition (SI) at high engine loads with advanced compression ignition (ACI) at low loads. To date, researchers have identified a number of potential fuel blendstocks that could provide the desired fuel properties.[1] These blendstocks include a broad range of functionalized hydrocarbons, such as alkenes, ketones, alcohols, and furans, which could be derived from biomass, further reducing overall petroleum consumption and greenhouse gas emissions. Newly developed engines and fuels bring new challenges for exhaust aftertreatment catalysts. On the one hand, varieties of blendstocks complicate hydrocarbon components in exhaust. On the other hand, the catalysts need to operate under both stoichiometric and lean-burn exhaust conditions as the engine switches between SI and ACI operation modes.

Platinum (Pt) has been widely studied for hydrocarbon and VOC (volatile organic compound) oxidation, because of its high activity.[2] Ceria (CeO_2) possesses high oxygen storage capacity (OSC) and redox properties due to the cycle of Ce^{4+}/Ce^{3+} redox pairs, making it an active support for oxidation catalysts. Combining these two materials, Pt/CeO_2-based catalyst systems have been widely applied as oxidation catalysts for automotive emission control.[3] The OSC of CeO_2-based catalysts is especially important for three-way catalysts (TWCs) which need to operate under rich-burn or stoichiometric conditions (low O_2). In addition, a strong metal–support interaction endows CeO_2-supported noble metal systems with unique redox activities. These features make Pt/CeO_2-based catalyst systems good candidates for addressing unburned hydrocarbon fuel exhaust for multimode engines.

Oxygen vacancy on CeO_2 plays a critical role in the oxidation activity of CeO_2-supported noble metal catalysts, as extensively reported for both CO[4–6] and hydrocarbon oxidation.[7–9] Specifically for HC oxidation on Pt/CeO_2 catalysts, Peng *et al.*[8] studied the effects of CeO_2 morphology

[a] *Institute for Integrated Catalysis, Pacific Northwest National Laboratory, P.O. Box 999, Richland, Washington 99354, USA. E-mail: yong.wang@pnnl.gov*
[b] *Voiland School of Chemical Engineering and Bioengineering, Washington State University, Pullman, Washington 99163, USA*

on the activity of Pt/CeO_2 for toluene oxidation. Three Pt/CeO_2 catalysts were synthesized using CeO_2 nanorods, nanoparticles, and nanocubes, which preferentially exposed the (110), (111), and (100) facets, respectively. The Pt/CeO_2-nanorods exhibit the best toluene oxidation activity, due to their highest concentration of surface oxygen vacancies. In addition, the reaction rates on the three catalysts were found to be proportional to the oxygen vacancy concentrations but independent of Pt dispersion, suggesting that the supply of active oxygen controls the reaction rate. The surface oxygen vacancies play a role in replenishing active oxygen species from the gaseous phase and accelerating the oxygen cycle for toluene oxidation. Wang and co-workers[9] modified a Pt/CeO_2-nanorod catalyst with dielectric barrier discharge plasma and significantly improved its activity for toluene oxidation (with T_{90} lowered by 79 °C). It was proposed that the improved activity is associated with the higher oxygen vacancy concentrations on the plasma-treated Pt/CeO_2 sample.

The redox activity of CeO_2 depends not only on the oxygen vacancy concentration but also on the structure of oxygen vacancies. Liu *et al.*[10] compared the CO oxidation activity of two types of CeO_2 nanorods with predominant exposure of the (100) + (111) and (100) + (110) facets, respectively. They found that the former containing large size oxygen vacancy clusters is more active than the latter predominated with isolated oxygen vacancies. Clusters of more than two vacancies, such as linear surface oxygen vacancies, proved to be favorable for migration of oxygen.[11]

Lee *et al.*[12] reported a simple approach for promoting the CO oxidation activity of Pt/CeO_2 by annealing the CeO_2 support at a high temperature of 800 °C before loading Pt. The high temperature pretreatment reduces the surface defects on CeO_2.[12,13] A low defect concentration leads to a weaker metal–support interaction on the Pt/CeO_2 catalyst and facilitates the formation of PtO_2 species, which is essential for the high CO oxidation ability. In this work, we applied a similar CeO_2 pre-annealing approach to synthesize a Pt/CeO_2 catalyst for hydrocarbon (HC) oxidation. We found that the HC oxidation activity is only related to the mobility of the surface lattice oxygen and not impacted by the morphology of Pt clusters.

Other than the activity of the catalysts, the identities of the target pollutants and the composition of the exhaust also significantly impact the performance of the after-treatment system. Previous work by ORNL[14,15] has showed how functionalities of fuel blendstocks might impact the performance of TWC systems in vehicles powered by spark-ignition (SI) engines under stoichiometric conditions. More information about the effects of fuel chemistry under lean-burn conditions is still lacking.

Therefore, in this work, we also investigated the effects of functional groups on the oxidation reactivity of hydrocarbon fuels on Pt/CeO_2 catalysts under various exhaust conditions. Under simulated exhaust conditions, where HC oxidation is suppressed by the competitive adsorption of NO and CO, fuel molecules, regardless of functionalities, are always more active under lean (high O_2) conditions than under rich (low O_2) conditions. The improved redox activity of Pt/CeO_2 benefits the HC oxidation by accelerating the rate-limiting O_2 activation step and broadening the operation window of an O dominant Pt surface. This simple approach for tuning the surface properties of CeO_2 can potentially be applied in other CeO_2-based systems for improved catalytic activities.

Experimental

Catalyst preparation

CeO_2-supported Pt catalysts were prepared by the incipient wetness impregnation method. Commercial CeO_2 (99.99%, 10 nm, US Research Nanomaterials, Inc.) was used as the support, and $[Pt(NH_3)_4](NO_3)_2$ (99.995%, Sigma Aldrich) as the Pt precursor. CeO_2 was either used as received or pre-calcined at 800 °C for 10 h in flowing air (zero grade) before loading the Pt precursor. The pre-calcined CeO_2 support is denoted $CeO_2(800)$, whereas the untreated CeO_2 is labelled $CeO_2(UT)$. An aqueous solution of $[Pt(NH_3)_4](NO_3)_2$ was impregnated on the respective CeO_2 supports to achieve a 1.5 wt% Pt loading. The Pt loaded CeO_2 samples were dried at 70 °C for 4 h and then calcined at 500 °C for 4 h in flowing air to obtain the Pt/CeO_2 catalysts. The catalyst samples are denoted as $Pt/CeO_2(UT)$ and $Pt/CeO_2(800)$, respectively.

Catalyst characterization

Powder X-ray diffraction (XRD) measurements were performed on a Philips PW3040/00 X'Pert powder X-ray diffractometer with CuKα radiation (λ = 1.5406 Å). Data were collected with 2θ ranging from 2° to 100° using a step size of 0.01°.

Transmission electron microscopy (TEM) measurements were conducted with an FEI Titan 80-300 operated at 300 kV. The observations were performed in scanning transmission electron micrscopy (STEM) mode using HAADF detector, as well as conventional TEM mode. All TEM images were digitally recorded using a charge-coupled device camera. The TEM specimens were prepared by dispersing the catalyst samples in ethanol and depositing the suspension onto a lacey carbon-coated copper grid.

Temperature-programed CO reduction (CO-TPR) was performed on a Micromeritics AutoChem II analyzer combined with an MSK Cirrus 2 mass spectrometer. About 70 mg of catalysts was loaded in the reactor for measurement. The samples were first pretreated in 10% O_2/He (50 cm^3 min^{-1}) at 250 °C for 30 min and then purged with He (50 cm^3 min^{-1}) at room temperature for 30 min. The first cycle of CO-TPR was performed in 1% CO/He (50 cm^3 min^{-1}) with a heating rate of 10 °C min^{-1} to 250 °C and held for 30 min. The second cycle of CO-TPR was performed with the same procedure and conditions, except the TPR temperature was increased to 500 °C.

Diffuse reflectance infrared Fourier transform spectroscopy (DRIFTS) studies of CO adsorption were performed on a Nicolet iS50R FT-IR spectrometer (Thermo Scientific) equipped with a liquid-nitrogen-cooled MCT detector and a Praying Mantis diffuse reflection accessory (Harrick Scientific Products Inc.) operated at a resolution of 4

cm^{-1}. The background spectra were collected with KBr powder in flowing He at 30 °C. Before measurements, the catalyst powders placed in the sample cell were pretreated by heating to 400 °C in 10% O_2/He (20 cm^3 min^{-1}) and holding for 30 min, followed by cooling down to 30 °C in flowing He (20 cm^3 min^{-1}). CO adsorption was performed with 1% CO/He (20 cm^3 min^{-1}). The samples were heated with a heating rate of 10 °C min^{-1} to 250 °C and held at 30, 50, 100, 150, 200, and 250 °C for 1 min for spectrum collection.

X-ray photoelectron spectroscopy (XPS) measurements of the pristine Pt/CeO_2(UT) and Pt/CeO_2(800) catalysts were performed on a Physical Electronics Quantera SXM scanning X-ray microprobe, with a focused monochromatic Al Kα X-ray (1486.7 eV) source for excitation and a spherical section analyzer. High energy resolution spectra were collected using a pass-energy of 69.0 eV with a step size of 0.125 eV. The binding energy (BE) scale was calibrated using the Cu $2p_{3/2}$ feature at 932.62 ± 0.05 eV and Au $4f_{7/2}$ at 83.96 ± 0.05 eV.

Catalyst activity evaluation

The catalyst activities for the oxidation of various hydrocarbon (HC) fuel blendstocks were evaluated by temperature-programed reaction using a plug flow microreactor system, with the reactor effluent composition quantified using an FTIR gas analyzer (MKS, Multigas 2030). The catalyst powders were pressed, crushed, and sieved (180–250 μm) for the tests. 150 mg of catalysts were mixed with 400 mg of SiC diluent and loaded in a quartz reactor (inner diameter ~10 mm) above a porous frit. The catalysts were tested under either fully simulated exhaust (containing HCs, O_2, H_2O, CO_2, CO, NO, H_2, and N_2 balance) or simplified conditions (containing HCs, O_2, and N_2 balance), as listed in Table 1, with a space velocity of 200 L g^{-1} h^{-1}. The simulated exhaust conditions are based on the U.S. DRIVE protocols LTC-G (low-temperature combustion with gasoline) and S-GDI (stoichiometric gasoline direct injection).[16] The concentrations of CO, NO, and H_2 were adjusted from the original protocols due to the limitation by the available gas mixture source (5000 ppm CO/2000 ppm NO/1000 ppm H_2). The liquid HC fuels and H_2O were introduced into vaporization zones located at the upstream of the reactor using a syringe infusion pump and an HPLC pump, respectively. The gas line was kept above 200 °C. In the light-off test, the reactor was heated with flowing air to 100 °C before switching to the testing gas feed and held for 10 min. Then, the temperature was ramped from 100 to 500 °C with a heating rate of 5 °C min^{-1}.

Kinetic measurements of steady state propene oxidation were performed using a plug flow microreactor system. 8–16 mg catalyst pellets (180–250 μm) were mixed with 400 mg of SiC and loaded in a quartz reactor (inner diameter ~10 mm) above a porous frit. The reaction was conducted isothermally at 220 °C. The reactant mixture consists of 500–3500 ppm propene and 2.5–15 vol% O_2 (balanced by He and N_2). The propene concentrations in the reactant feed and reactor effluent were quantified using a gas chromatograph (Agilent, 7890A) equipped with a capillary column (Agilent HP-1, 19091Z-433, 30 m, 0.25 mm ID, 0.25 μm film) connected to a flame ionization detector (FID). The rate of propene oxidation was determined based on the propene concentration difference between the reactant feed and reactor effluent.

Table 1 Gas composition for the catalyst tests

Gas components	Concentration			
	LTC-G	S-GDI	High O_2	Low O_2
O_2	10%	0.74%	10%	0.74%
H_2O	6%	13%	—	—
CO_2	6%	13%	—	—
CO	2000 ppm	3500 ppm	—	—
NO	800 ppm	1400 ppm	—	—
H_2	400 ppm	700 ppm	—	—
HCs	3000 ppm C_1	3000 ppm C_1	3000 ppm C_1	3000 ppm C_1

Results and discussion

Influence of CeO_2 calcination on the structure of Pt/CeO_2 catalysts

Fig. 1 shows the XRD patterns of the CeO_2 supports and Pt/CeO_2 catalysts. The high temperature calcination caused crystalline growth (Table 2) and thus the sharpening of the CeO_2 diffraction peaks. Correspondingly, the surface area of the support decreases from 82 m^2 g^{-1} on the untreated CeO_2(UT) to 18 m^2 g^{-1} on the 800 °C-calcined CeO_2(800) (Table 2). No phase change was observed. Pt clusters were formed on both Pt/CeO_2 catalysts, as indicated by the presence of a weak Pt (111) peak at 40°.

The CeO_2 calcination impacted the morphology of the loaded Pt clusters. Fig. 2 shows the TEM images and the Pt nanoparticle size distributions of Pt/CeO_2(UT) and Pt/CeO_2(800). On the untreated CeO_2(UT), Pt formed nanoparticles with sizes of around 1–2 nm (Fig. 2a). On the high temperature treated CeO_2(800), although the XRD spectrum indicates the existence of Pt nanoparticles (Fig. 1),

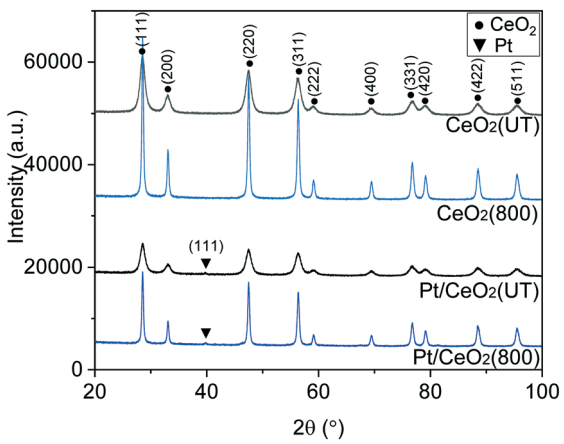

Fig. 1 XRD profiles of the CeO_2 supports and Pt/CeO_2 catalysts.

Table 2 Properties of the CeO_2 supports and Pt/CeO_2 catalysts

Sample	Surface area[a] (m^2 g^{-1})	Pt loading[b] (wt%)	CeO_2 crystalline size[c] (nm)
CeO_2(UT)	82	—	7.7
CeO_2(800)	27	—	23.0
Pt/CeO_2(UT)	82	1.54	8.0
Pt/CeO_2(800)	30	1.66	23.4

[a] Measured by the BET method. [b] Measured by ICP. [c] Determined by XRD.

TEM shows that Pt particles were predominantly highly dispersed as two-dimensional monolayer clusters (Fig. 2b). However, these monolayer Pt clusters were not stable. Upon reductive treatment with CO at 250 °C, Pt aggregated to form small nanoparticles with a size of 1–1.5 nm (Fig. 2c). The Pt nanoparticles on Pt/CeO_2(800), however, show much more active redox properties than those on Pt/CeO_2(UT).

Influence of CeO_2 calcination on the redox activity of Pt/CeO_2 catalysts

The redox properties of the Pt/CeO_2 catalysts were examined with CO-TPR. As shown in Fig. 3a, in the first cycle of CO-TPR to 250 °C, the reduction of the pristine Pt/CeO_2(UT) initiates at around 100 °C and reached maximum at 125 °C. This low temperature reduction peak is associated with the CeO_2 surface lattice oxygen activated by Pt nanoparticles. In the second cycle of CO-TPR to 400 °C, the as-reduced Pt/CeO_2(UT) shows a lower reduction peak temperature at 105 °C. A second reduction peak appears at 250 °C, which is assigned to CeO_2 surface lattice oxygen not activated by Pt,[10,17] as bare CeO_2(UT) support also shows a weak reduction peak at the same temperature (Fig. 3a).

The 800 °C pretreatment of the CeO_2 support promoted the redox properties of the Pt/CeO_2 catalyst. As shown in Fig. 3b, in the first CO-TPR cycle, the reduction of the pristine Pt/CeO_2(800) initiates below 50 °C, with the first reduction peak centered at 79 °C. Again, this low temperature reduction is assigned to surface CeO_2 lattice oxygen activated by Pt clusters. Similar high redox properties of Pt/CeO_2 have previously been reported by Lee and co-workers,[12] who also reported that a Pt/CeO_2 catalyst using a 800 °C-pretreated CeO_2 support showed a low temperature reduction peak at 60 °C in H_2-TPR, in comparison to the 165 °C reduction peak for a Pt/CeO_2 sample with untreated CeO_2 support. The pristine Pt/CeO_2(800) has a second reduction peak at 120 °C, which is ascribed to lattice oxygen activated by atomically dispersed Pt atoms.[6] In the second CO-TPR cycle to 400 °C, the reduced Pt/CeO_2(800) only showed one low temperature reduction peak at 81 °C associated with Pt clusters, as the Pt single-atoms had aggregated to Pt clusters in the first CO-TPR cycle, as confirmed by TEM (Fig. 2c). Both the pristine Pt/CeO_2(800) with 2D Pt rafts and the reduced Pt/CeO_2(800) with 3D Pt particles show a similar low temperature reduction peak (79–81 °C), indicating that the morphology of the Pt clusters only has minor effects on the high redox activity of Pt/CeO_2(800) reflected by CO-TPR.

It is noted that the Pt/CeO_2(800) sample does not show any additional reduction peak at around 250 °C related to unactivated surface lattice oxygen as observed on Pt/CeO_2(UT), although the bare CeO_2(800) support does have a weak reduction peak at around 250 °C. We postulate that all the reducible surface lattice oxygen species on CeO_2(800) can easily migrate to the Pt clusters to react with CO within the first reduction peak at around 80 °C.

The state of the Pt species on the Pt/CeO_2 samples was further investigated by *in situ* DRIFTS of the CO adsorption during and after CO-TPR. As shown in Fig. 4a, during CO-TPR starting at 30 °C, the as-calcined Pt/CeO_2(UT) sample shows a peak at 2096 cm^{-1} for CO adsorption on ionic $Pt^{\delta+}$,[6,18] as the Pt cluster surfaces are either covered with PtO_x or chemisorbed O. As the temperature increases to 100 °C, a

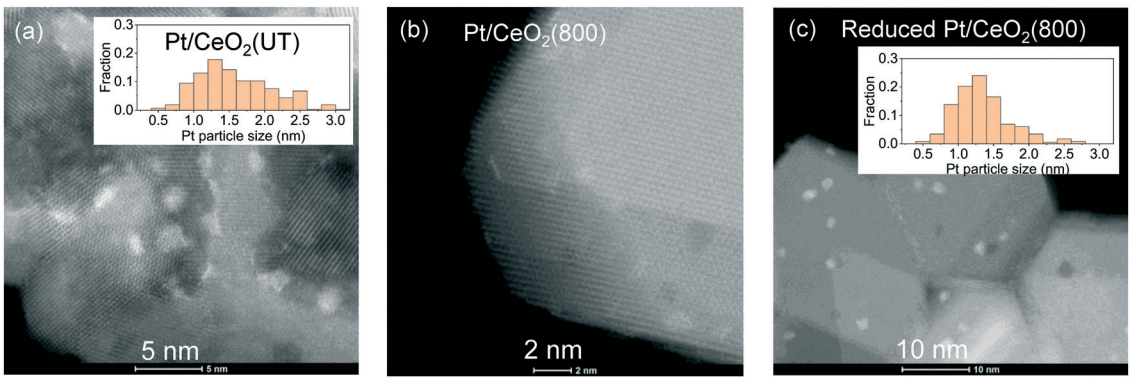

Fig. 2 STEM HAADF images and Pt particle size distributions of (a) Pt/CeO_2(UT), (b) Pt/CeO_2(800), and (c) reduced Pt/CeO_2(800).

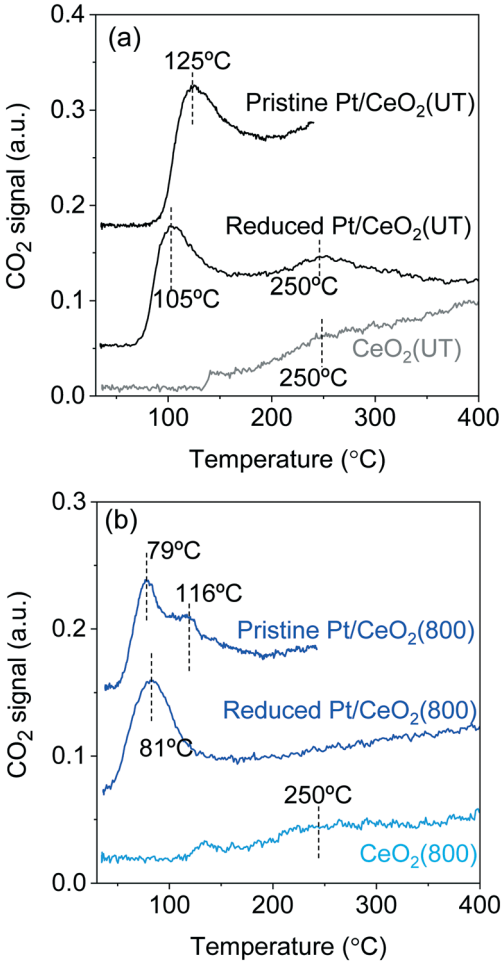

Fig. 3 CO-TPR profiles of the pristine and reduced (a) $Pt/CeO_2(UT)$ and (b) $Pt/CeO_2(800)$ (after the first CO-TPR of the pristine catalysts to 250 °C in 1% CO/He and being held for 30 min; the reduced catalysts were re-oxidized at 250 °C in 10% O_2/He for 30 min before the second cycle of CO-TPR).

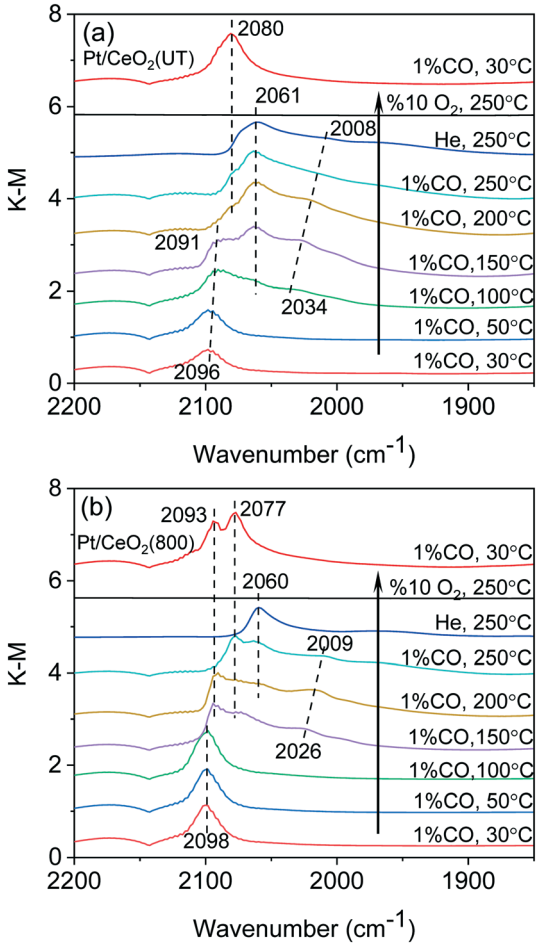

Fig. 4 DRIFTS spectra of CO adsorption on (a) $Pt/CeO_2(UT)$ and (b) $Pt/CeO_2(800)$ during and after CO-TPR to 250 °C.

band at 2061 cm^{-1} and a broad tail with lower frequencies (2060–1950 cm^{-1}) appeared, which are assigned to linearly adsorbed CO on metallic Pt^0 atoms with different coordination numbers,[6,18] indicating the initiated reduction of the Pt species by CO at this temperature. Therefore, the reduction peak of the pristine $Pt/CeO_2(UT)$ sample in Fig. 3 at 130 °C is accompanied by the reduction of the Pt clusters. As the temperature further increases, the ionic $Pt^{\delta+}$ (2091–2096 cm^{-1}) gradually disappears accompanied by the growth of metallic Pt (2061 cm^{-1}). After the re-oxidation treatment at 250 °C and cooling to 30 °C, CO adsorption on the catalyst shows a peak at 2080 cm^{-1}, which is assigned to the co-adsorption of CO and oxygen on the Pt clusters.[18]

For $Pt/CeO_2(800)$, the as-calcined sample also shows a peak at 2098 cm^{-1} for the CO adsorption on ionic $Pt^{\delta+}$ (ref. 6 and 18) at room temperature. These ionic $Pt^{\delta+}$ species remain stable during CO-TPR up to 100 °C, and metallic Pt species appear at 150 °C, 50 °C higher than for $Pt/CeO_2(UT)$ (Fig. 4a). Since no reduction of $Pt^{\delta+}$ species occurs on pristine $Pt/CeO_2(800)$ at 100 °C, the reduction peak at 70 °C must be exclusively associated with the consumption of lattice oxygen from the $CeO_2(800)$ support. As the reduction temperature increases above 150 °C, the appearance of metallic Pt species (2077, 2060, and 2020–2009 cm^{-1}) is associated with the aggregation of two-dimensional Pt rafts (Fig. 2b) to three-dimensional Pt nanoclusters (Fig. 2c). After the re-oxidation at 250 °C and cooling to 30 °C for CO adsorption, the $Pt/CeO_2(800)$ sample presents two peaks at 2077 and 2093 cm^{-1}, respectively. Although the former is associated with the co-adsorption of CO and oxygen on the Pt clusters, similar to that on $Pt/CeO_2(UT)$, the latter is assigned to the ionic $Pt^{\delta+}$ species, suggesting that Pt is easier to be oxidized on $Pt/CeO_2(800)$. The lower reduction temperature of CeO_2 surface lattice oxygen than that of PtO_x, together with the ease of PtO_x formation, suggests a strong metal–support interaction on this catalyst. In addition, the pristine and reduced $Pt/CeO_2(800)$ have different Pt oxidation states (Fig. 4b) but similar redox activity (Fig. 3b), indicating that the oxidation states of the Pt clusters (except Pt single atoms) do not influence the redox activity of $Pt/CeO_2(800)$. Therefore, we postulated that the redox activity was related to the nature of the CeO_2 support.

The TEM images (Fig. 2b and c) show that the CeO_2(800) support consists of larger CeO_2 particles with the well-defined (111) facet exposed. In contrast, the untreated CeO_2(UT) support (Fig. 2a) has a less defined morphology. Another difference between these two CeO_2 supports is the surface carbonate species. Fig. 5 shows the DRIFTS spectra of the carbonate/bicarbonate species on the two supports CeO_2(500) (prepared by calcining CeO_2(UT) at 500 °C in flowing air for 4 h) and CeO_2(800) and two catalysts Pt/CeO_2(UT) and Pt/CeO_2(800). The surfaces of CeO_2(500) and Pt/CeO_2(UT) contain much more carbonate species than those of CeO_2(800) and Pt/CeO_2(800), including monodentate (1464 cm^{-1}), polydentate (1395 cm^{-1}), and bidentate (1301 cm^{-1}) carbonate species.[19–22] These carbonate species are likely formed by the adsorption of CO_2 on the defect sites on the CeO_2 surface. The carbonate species on CeO_2(UT) are very stable, as they cannot be removed by 400 °C pretreatment in 10% O_2/He. The CeO_2(800) and Pt/CeO_2(800) surfaces mainly contain less stable bicarbonate species (3609 and 1607 cm^{-1}).[19–22] There are two possible reasons for the much lower surface carbonate concentration on CeO_2(800): (1) the high temperature calcination (800 °C for 10 h) decreases the amount of surface defects; (2) CeO_2(800) predominantly exposes the (111) facet which is much less favorable for CO_2 adsorption in comparison to the (100) and (110) facets.[23] The lower surface defect density on the high temperature treated sample was further confirmed by XPS. Fig. 6 shows the O1s XPS spectra of the pristine Pt/CeO_2(UT) and Pt/CeO_2(800) catalysts. The peaks at 529.3, 530.6, and 532.8 eV are associated with CeO_2 lattice oxygen, CeO_2 surface defects/PtO_x oxygen, and adsorbed water/other adsorbed species, respectively.[24] Given a similar amount of PtO_x species on these two catalysts, a smaller peak of Pt/CeO_2(800) at 530.6 eV than that of Pt/CeO_2(UT) indicates a lower amount of surface defects on the former.

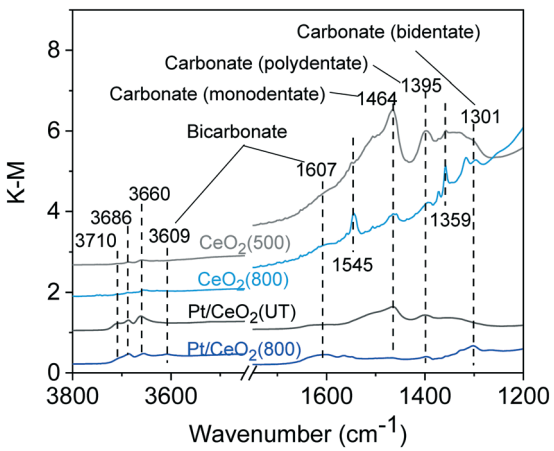

Fig. 5 DRIFTS spectra of carbonated/bicarbonate species on the two supports CeO_2(500) (prepared by calcining CeO_2(UT) at 500 °C in flowing air for 4 h) and CeO_2(800) and two catalysts Pt/CeO_2(UT) and Pt/CeO_2(800) at 80 °C (all the samples were pretreated with 10% O_2/He at 400 °C for 30 min before cooling down to 80 °C for spectrum collection).

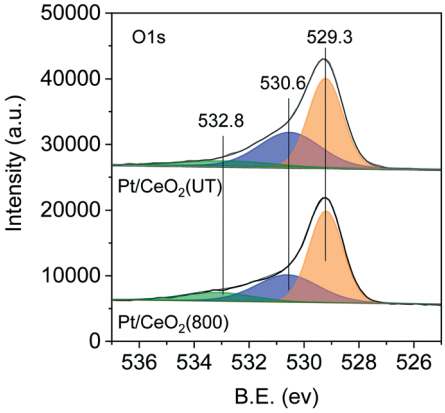

Fig. 6 O1s XPS spectra of the pristine Pt/CeO_2(UT) and Pt/CeO_2(800) catalysts.

The high redox activity of Pt/CeO_2(800) is likely related to much lower carbonate concentrations on the CeO_2(800) support. It's been widely accepted that the redox properties of CeO_2 is associated with the surface oxygen vacancies.[10,11,25] The migration of oxygen in CeO_2 takes place *via* a vacancy hopping mechanism.[10,26] We postulated that the formation of stable carbonates on the surface defects likely hinders the hopping of oxygen vacancies along the CeO_2 surface. Therefore, oxygen migration is more favorable on the CeO_2(800) surface which contains much less stable carbonate species. CO-TPR (Fig. 3) cannot reflect the difference between the bare CeO_2(UT) and CeO_2(800) supports, simply because the CeO_2 lattice oxygen requires Pt species as active sites to react with CO.

Catalytic activity for HC oxidation

The catalytic performance of Pt/CeO_2(UT) and Pt/CeO_2(800) for HC oxidation was evaluated with selected fuel blendstock components with different functional groups. Fig. 7a shows the T_{50} and T_{90} (temperatures of 50% and 90% conversion, respectively) values for the light-off of 8 fuel components on Pt/CeO_2(800) under different simplified and simulated test conditions (as listed in Table 1). Under simplified conditions with 0.74% or 10% O_2, the functional group of the fuel molecule largely impacts its oxidation reactivity. The unfunctionalized alkanes (isooctane and *n*-heptane) are more reactive (with lower T_{50} and T_{90}) in low O_2 (0.74%) than in high O_2 (10%), whereas all the functionalized HCs with C=C, C–O, or C=O show a reverse trend, being more reactive under a high O_2 condition. This is associated with the competitive adsorption between O_2 and fuel molecules on the Pt catalysts. The unfunctionalized alkanes adsorb relatively weakly on Pt. Therefore, under high O_2 pressure (10%), the Pt surface is predominated by oxygen species with low coverage of alkanes, resulting in a low reaction rate. On this O-dominated Pt surface, reducing the O_2 pressure increases the alkane coverage and promotes the reaction rate. In contrast, the functionalized HC molecules (with C=C, C–

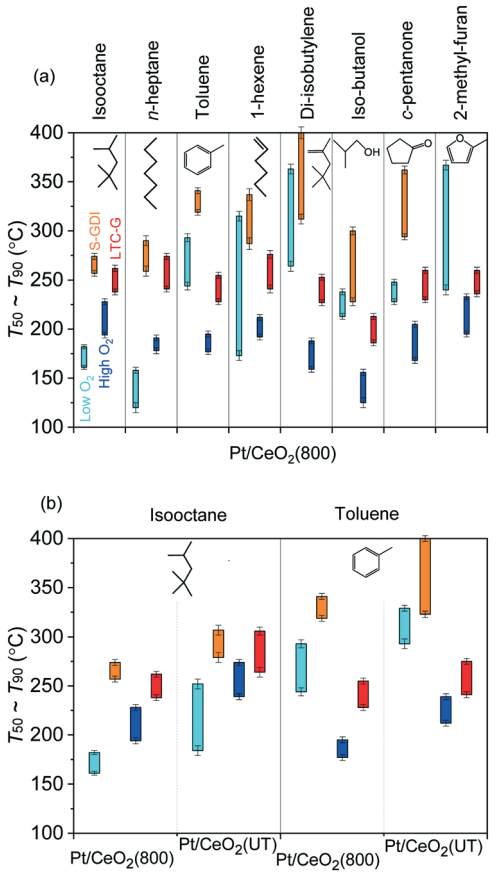

Fig. 7 (a) T_{50} and T_{90} (temperatures of 50% and 90% conversion) for the oxidation of selected fuel components on the $Pt/CeO_2(800)$ catalyst under different simulated or simplified exhaust conditions; (b) comparison of T_{50} and T_{90} for isooctane and toluene oxidation on the $Pt/CeO_2(800)$ and $Pt/CeO_2(UT)$ catalysts under different conditions (space velocity = 200 L g^{-1} h^{-1}; gas compositions are summarized in Table 1; all the catalysts were reduced by 1% CO/N_2 at 250 °C before the test).

O, or C═O) adsorb strongly on Pt, leading to an HC-dominated surface with low oxygen coverage, so the oxidation reaction is limited by the availability of active O species. In this case, increasing the O_2 pressure promotes the reaction rate.

Under the simulated stoichiometric (S-GDI) and lean (LTC-G) conditions, the T_{50} and T_{90} values of all the fuel components are significantly increased, in comparison to the corresponding simplified conditions (0.74% and 10% O_2, respectively), as shown in Fig. 7a. This is the well-known inhibition effects of other exhaust components (CO, NO, and H_2O) on HC oxidation over Pt catalysts, associated with adsorption competition.[27,28]

We selected isooctane and toluene as representative fuel components with weak and strong adsorption, respectively, to compare the catalytic performance of $Pt/CeO_2(UT)$ and $Pt/CeO_2(800)$. As shown in Fig. 7b, for both isooctane and toluene, $Pt/CeO_2(800)$ shows lower T_{50} and T_{90} than $Pt/CeO_2(UT)$ under all the conditions.

We rule out Pt dispersion or Pt morphology to be the reason for the high activity of $Pt/CeO_2(800)$. As shown in

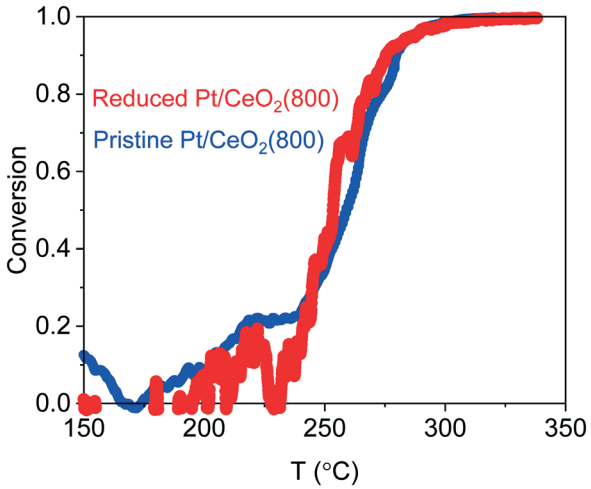

Fig. 8 Light-off curves for the isooctane oxidation on the pristine and reduced $Pt/CeO_2(800)$ catalysts (light-off condition: S-GDI; catalyst reduction treatment conditions: 1% CO/He, 250 °C, 30 min).

Fig. 8, the light-off curves for the isooctane oxidation on the pristine $Pt/CeO_2(800)$ with 2D Pt rafts (Fig. 2b) and the reduced $Pt/CeO_2(800)$ with 3D Pt particles (Fig. 2c) almost overlap, indicating that the morphology of the Pt clusters does not influence the HC oxidation activity. On the other hand, $Pt/CeO_2(UT)$ (Fig. 2a) and $Pt/CeO_2(800)$ (Fig. 2c) have close Pt particle sizes (1.5–2 nm) and thus similar Pt dispersion. Therefore, the high HC oxidation activity of $Pt/CeO_2(800)$ is likely related to its high redox activity. Next, we applied more rigorous kinetic measurements of propene oxidation to gain more insights into the superior activity of $Pt/CeO_2(800)$ for HC oxidation.

Kinetic insights into the influence of redox activity on HC oxidation on Pt/CeO_2

To better understand the promoted HC oxidation activity of $Pt/CeO_2(800)$ in comparison to $Pt/CeO_2(UT)$, we examined the kinetic dependence of propene (C_3H_6) oxidation on these two catalysts. We fixed the O_2 partial pressure and varied the C_3H_6 pressure. As shown in Fig. 9, under a specific O_2 pressure, as the C_3H_6 pressure (or C_3H_6/O_2 ratio) increases, the rate of C_3H_6 oxidation first increases and then decreases. Such kinetic dependence transition is due to the change of relative coverage of oxygen and HC species on the Pt surface, as previously reported for HC (*e.g.*, methane, propane) oxidation on Pt/Al_2O_3 catalysts.[29,30] With a low C_3H_6/O_2 ratio, the Pt surface is predominated by O species, and the total oxidation rate is limited by the availability of activated C_3H_6. Thus, increasing the C_3H_6/O_2 ratio and C_3H_6 coverage will increase the oxidation rate. Under a high C_3H_6/O_2 ratio, the Pt surface is predominantly covered by C_3H_6 and the oxidation rate is limited by the availability of activated oxygen species, so further increasing C_3H_6/O_2 decreases the oxidation rate.

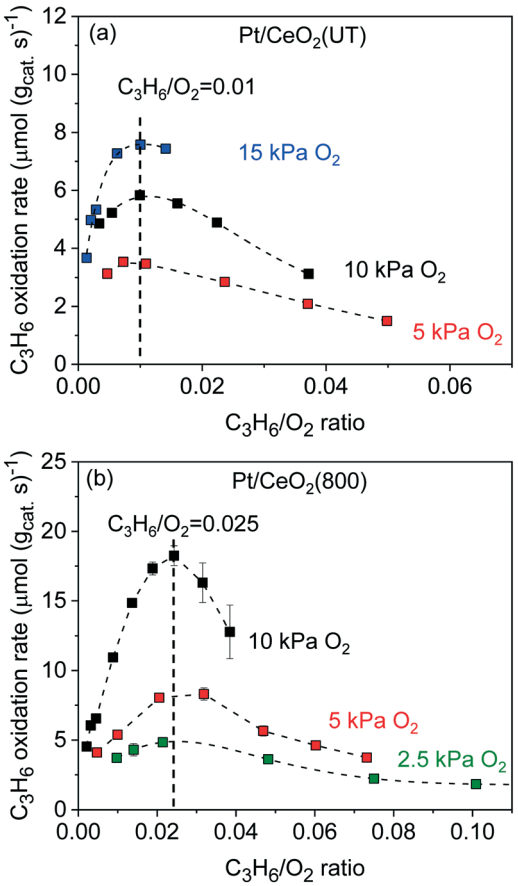

Fig. 9 Rates of propene oxidation on (a) Pt/CeO_2(UT) and (b) Pt/CeO_2(800) as a function of C_3H_6-to-O_2 ratio (220 °C).

It is noted that, regardless of the O_2 pressure, the C_3H_6/O_2 ratio for the kinetic regime transition remains constant (0.01 on Pt/CeO_2(UT) and 0.025 on Pt/CeO_2(800), respectively), suggesting that under this condition the Pt surface is fully covered by oxygen and C_3H_6 species and is free of bare Pt sites. In other words, under a fixed C_3H_6/O_2 ratio (*e.g.*, 0.01 for Pt/CeO_2(UT)), increasing the O_2 pressure does not change the coverage of C_3H_6 or oxygen species on the Pt surface. However, the C_3H_6 oxidation rate still increases with increasing O_2 pressure. Such a positive reaction order on O_2 pressure under constant Pt surface species coverage indicates that the rate of C_3H_6 oxidation is not limited by the Langmuir–Hinshelwood reaction between the activated C_3H_6 and oxygen species on the Pt surface. Instead, the kinetically relevant step appears to proceed either *via* the Eley–Rideal mechanism occurring between a C_3H_6-derived intermediate on the Pt surface and gas phase oxygen or *via* the Mars–van Krevelen mechanism between a C_3H_6-derived intermediate and active oxygen from the CeO_2 surface (lattice oxygen). Both the mechanisms show a positive reaction order under O_2 pressure.[31] This phenomenon is in line with previous discovery by Peng and co-workers,[8] who demonstrated that oxygen species for toluene oxidation on Pt/CeO_2 catalysts is supplied by the surface lattice oxygen of the CeO_2 support and the rate-limiting step for toluene oxidation on Pt/CeO_2 catalysts is the activation of oxygen species at the oxygen vacancies of the CeO_2 surface, as they observed that the rates of toluene oxidation over three Pt/CeO_2 catalysts with different CeO_2 morphologies are not relevant to the Pt dispersion but proportional to the oxygen vacancy concentrations on CeO_2. In this work, the high HC oxidation activity of Pt/CeO_2(800) is likely associated with its high mobility of surface lattice oxygen as demonstrated by CO-TPR (Fig. 3b).

It is also noted that the C_3H_6/O_2 ratio for the transition from the oxygen-dominated surface to the HC-dominated surface is higher on Pt/CeO_2(800) than on Pt/CeO_2(UT) (0.025 *vs.* 0.01). This indicates that the high lattice oxygen mobility of Pt/CeO_2(800) increases the chemical potential of oxygen species on the Pt surface and broadens the operation window of the oxygen-dominated surface, which is beneficial for the catalyst operation under rich conditions.

Conclusions

High temperature (800 °C) pretreatment of CeO_2 support before loading Pt significantly promotes the redox activity of Pt/CeO_2 catalysts. The improved redox activity is not related to the structure or oxidation state of Pt clusters. Instead, it is likely associated with the lower amount of surface defects on the 800 °C-treated CeO_2 support. The low-defect surface favors the mobility of lattice oxygen and thus improves the redox activity of Pt/CeO_2 catalysts.

The Pt/CeO_2 catalysts were evaluated in the oxidation of a series of hydrocarbon fuel molecules under various conditions. The functional groups (C═C, C–O, and C═O bonds) of the fuel molecules affect their adsorption strengths and thus the oxidation reactivities under different conditions. Under simplified conditions with only O_2 and fuel molecules, the unfunctionalized alkanes, which adsorb relatively weakly on Pt catalysts, are more reactive under stoichiometric (low O_2) conditions than under lean (high O_2) conditions, whereas all the functionalized (by C═C, C–O, and C═O) fuel molecules with stronger adsorption show a reverse trend, being more reactive under lean conditions. Under simulated conditions, the presence of NO and CO suppresses the oxidation reactivities of all fuel molecules by competitive adsorption. In this case, all fuel molecules are more reactive under lean (LTC-G, high O_2) conditions than under stoichiometric (S-GDI, low O_2) conditions.

The Pt/CeO_2 catalyst with 800 °C-treated CeO_2 support presents promoted catalytic activity for HC oxidation, for both weakly-adsorbed alkanes (represented by isooctane) and strongly-adsorbed aromatics (represented by toluene), under both lean and stoichiometric conditions. Such improved HC oxidation activity is associated with the promoted redox activity. Kinetic measurement indicates that the promoted redox activity benefits the HC oxidation reaction in two ways: (1) accelerating the kinetically-relevant O_2 activation step and (2) increasing the oxygen chemical potential on Pt clusters so

as to broaden the operation window of an oxygen-dominant Pt surface.

Author contributions

Fan Lin: methodology, investigation, formal analysis, and writing – original draft. Kenneth Rappé: investigation. Libor Kovarik: investigation. Miao Song: investigation. Xiaohong Shari Li: investigation. Mark Engelhard: investigation. Yong Wang: funding acquisition, project administration, conceptualization, methodology, and writing – review & editing.

Conflicts of interest

There are no conflicts to declare.

Acknowledgements

This work was sponsored by the US Department of Energy (DOE), Vehicle Technologies Office under the DOE Co-optimization of Fuels and Engines Initiative. A part of the research described in this paper was performed in the Environmental Molecular Sciences Laboratory (EMSL), a national scientific user facility sponsored by the DOE's Office of Biological and Environmental Research and located at PNNL. PNNL is operated for the US DOE by Battelle.

References

1 D. J. Gaspar, B. H. West, D. Ruddy, T. J. Wilke, E. Polikarpov, T. L. Alleman, A. George, E. Monroe, R. W. Davis, D. Vardon, A. D. Sutton, C. M. Moore, P. T. Benavides, J. Dunn, M. J. Biddy, S. B. Jones, M. D. Kass, J. A. Pihl, M. M. Debusk, M. Sjoberg, J. Szybist, C. S. Sluder, G. Fioroni and W. J. Pitz, Top Ten Blendstocks Derived From Biomass For Turbocharged Spark Ignition Engines: Bio-blendstocks With Potential for Highest Engine Efficiency, United States, 2019.
2 L. F. Liotta, *Appl. Catal., B*, 2010, **100**, 403–412.
3 M. A. Salaev, A. A. Salaeva, T. S. Kharlamova and G. V. Mamontov, *Appl. Catal., B*, 2021, **295**, 120286.
4 S. Chang, M. Li, Q. Hua, L. Zhang, Y. Ma, B. Ye and W. Huang, *J. Catal.*, 2012, **293**, 195–204.
5 N. Singhania, E. A. Anumol, N. Ravishankar and G. Madras, *Dalton Trans.*, 2013, **42**, 15343–15354.
6 X. I. Pereira-Hernández, A. DeLaRiva, V. Muravev, D. Kunwar, H. Xiong, B. Sudduth, M. Engelhard, L. Kovarik, E. J. M. Hensen, Y. Wang and A. K. Datye, *Nat. Commun.*, 2019, **10**, 1358.
7 H. Huang, Q. Dai and X. Wang, *Appl. Catal., B*, 2014, **158-159**, 96–105.
8 R. Peng, X. Sun, S. Li, L. Chen, M. Fu, J. Wu and D. Ye, *Chem. Eng. J.*, 2016, **306**, 1234–1246.
9 B. Wang, B. Chen, Y. Sun, H. Xiao, X. Xu, M. Fu, J. Wu, L. Chen and D. Ye, *Appl. Catal., B*, 2018, **238**, 328–338.
10 X. Liu, K. Zhou, L. Wang, B. Wang and Y. Li, *J. Am. Chem. Soc.*, 2009, **131**, 3140–3141.
11 F. Esch, S. Fabris, L. Zhou, T. Montini, C. Africh, P. Fornasiero, G. Comelli and R. Rosei, *Science*, 2005, **309**, 752–755.
12 J. Lee, Y. Ryou, J. Kim, X. Chan, T. J. Kim and D. H. Kim, *J. Phys. Chem. C*, 2018, **122**, 4972–4983.
13 Q. Fu, H. Saltsburg and M. Flytzani-Stephanopoulos, *Science*, 2003, **301**, 935–938.
14 S. Sinha Majumdar, J. A. Pihl and T. J. Toops, *Appl. Energy*, 2019, **255**, 113640.
15 S. Sinha Majumdar and J. A. Pihl, *Energy Fuels*, 2020, **34**, 12900–12910.
16 K. G. Rappé, C. DiMaggio, J. A. Pihl, J. R. Theis, S. H. Oh, G. B. Fisher, J. Parks, V. G. Easterling, M. Yang, M. L. Stewart and K. C. Howden, *Emiss. Control Sci. Technol.*, 2019, **5**, 183–214.
17 A. A. Voskanyan, C.-K. J. Tsui and K.-Y. Chan, *J. Catal.*, 2020, **382**, 155–164.
18 P. Bazin, O. Saur, J. C. Lavalley, M. Daturi and G. Blanchard, *Phys. Chem. Chem. Phys.*, 2005, **7**, 187–194.
19 Z. Wu, A. K. P. Mann, M. Li and S. H. Overbury, *J. Phys. Chem. C*, 2015, **119**, 7340–7350.
20 M. Li, U. Tumuluri, Z. Wu and S. Dai, *ChemSusChem*, 2015, **8**, 3651–3660.
21 U. Tumuluri, G. Rother and Z. Wu, *Ind. Eng. Chem. Res.*, 2016, **55**, 3909–3919.
22 C. Li, Y. Sakata, T. Arai, K. Domen, K.-I. Maruya and T. Onishi, *J. Chem. Soc., Faraday Trans. 1*, 1989, **85**, 929–943.
23 A. R. Symington, R. M. Harker, M. T. Storr, M. Molinari and S. C. Parker, *J. Phys. Chem. C*, 2020, **124**, 23210–23220.
24 A. I. Stadnichenko, V. V. Muravev, S. V. Koscheev, V. I. Zaikovskii, H. A. Aleksandrov, K. M. Neyman and A. I. Boronin, *Surf. Sci.*, 2019, **679**, 273–283.
25 C. T. Campbell and C. H. F. Peden, *Science*, 2005, **309**, 713–714.
26 C. R. A. Catlow, *J. Chem. Soc., Faraday Trans.*, 1990, **86**, 1167–1176.
27 K. Daneshvar, R. Krishna Dadi, D. Luss, V. Balakotaiah, S. B. Kang, C. M. Kalamaras and W. S. Epling, *Chem. Eng. J.*, 2017, **323**, 347–360.
28 S. E. Voltz, C. R. Morgan, D. Liederman and S. M. Jacob, *Product R&D*, 1973, **12**, 294–301.
29 C. P. O'Brien, G. R. Jenness, H. Dong, D. G. Vlachos and I. C. Lee, *J. Catal.*, 2016, **337**, 122–132.
30 Y.-H. Chin, C. Buda, M. Neurock and E. Iglesia, *J. Am. Chem. Soc.*, 2011, **133**, 15958–15978.
31 J. R. H. Ross, in *Contemporary Catalysis*, ed. J. R. H. Ross, Elsevier, Amsterdam, 2019, pp. 161–186, DOI: 10.1016/B978-0-444-63474-0.00007-2.